Electrosynthesis of Iron, Cobalt, and Zinc Microcrystals and Magnetic Enhancement of the Oxygen Reduction Reaction

Lorena M. A. Monzon,* Karsten Rode, M. Venkatesan, and J.M.D. Coey

School of Physics, Trinity College, Dublin 2, Ireland

S *Supporting Information*

ABSTRACT: Sparse metallic crystals of iron, cobalt, and zinc are produced by electrodeposition on polyaniline (PANI) coated gold electrodes. The crystal habit is determined by the composition of the electrolyte. Thin hexagonal crystallites of cobalt or zinc can grow with the basal plane parallel to the substrate, but acetic acid strongly affects the growth of the cobalt deposits, as it changes the crystal habit from hexagonal to hemispherical. Iron is electrodeposited on PANI in the form of submicrometer cubes in the presence of acetic acid, while in its absence micrometer-size hemispheres are produced. The magnetization curves for Fe and Co are correlated with the observed textures. Sparse heterogeneously structured surfaces with ~2 μm hemispherical metal grains of the three metals were then used as electrodes to investigate the magnetic field effect on the oxygen reduction reaction. For zinc, the effect of a 360 mT applied magnetic field was a slight increase (3%) in the maximum oxygen reduction current, which is attributed to magnetohydrodynamic (MHD) flows produced by the interaction of the external magnetic field and the current distribution near the surface of the grains via the Lorentz force. Significantly larger increases, ~12% and ~8% for iron and cobalt, respectively, are attributed to enhanced convection in the vicinity of the ferromagnetic grains due to the magnetic field gradient force.

KEYWORDS: *polyaniline, Fe, Co, and Zn crystals, magnetoelectrochemistry, oxygen reduction reaction*
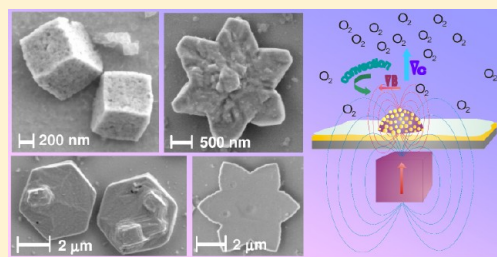
1. INTRODUCTION

There have been several studies of electroless deposition of metallic particles on polyaniline (PANI) films,[1−3] where the noble metal cations present in solution (Au, Pt, Ag) spontaneously oxidize PANI while they nucleate and grow at the polymer surface. It has been shown that the shape and size of the metallic particles obtained can be controlled by the nature of the acid employed to dope the polymer.[2] Copper based clusters have also been deposited on PANI by electrochemical techniques,[4,5] whereby their morphology is modified by the electrochemical parameters employed during the crystal growth. However, to the best of our knowledge, the deposition of transition metal particles on conducting polymers has not been described. The physicochemical aspects of this process are expected to be different from that for noble metals, as it takes place in the potential region where PANI becomes highly insulating.[6]

In this paper, transition metal particles are grown under several experimental conditions, and the factors governing nucleation and growth, shape, crystal structure, and magnetic properties are analyzed. These submicrometer to micrometer sized crystals of iron, cobalt, and zinc produced electrochemically are then used to evaluate the effect of localized magnetic fields on the electrochemical oxygen reduction reaction, where paramagnetic molecular O_2 is reduced to water.

It is known that a uniform magnetic field **B** can interact with the electric current density **j** in an electrochemical cell producing a local Lorentz force $\mathbf{F}_L = \mathbf{j} \times \mathbf{B}$, which creates convection that modifies the distribution of the charged species near the surface of the electrode. The effect is a local stirring that improves the mass transport of ions toward the electrode surface. This force is maximum when **j** and **B** are orthogonal. If the magnetic field is not uniform, it induces a nonuniform magnetization in the electrolyte solution and it exerts a force on the induced moment of any paramagnetic species.[7−9] A magnetic gradient is able to induce a local convective flow via the Kelvin force $\mathbf{F}_K = (1/2 \mu_0)\chi \nabla B^2$ when it is orthogonal to the paramagnetic concentration gradient.[10−13] Here, χ is the magnetic susceptibility of the electrolyte. When a concentration gradient is established, there is an enhanced flow of electrolyte rich in paramagnetic species toward regions of high magnetic field at the electrode surface that result in a net increase of the local current. In electrodeposition, it is found that these gradients modify the thickness of the diffusion layer, and electrodeposits of paramagnetic ions are produced as a result of magnetic pressure[10,11] So far, millimeter size permanent magnets or soft magnets and external magnetic fields have been used to produce magnetic field gradients on a working electrode.[7−13] Arrays of magnetic nanowires embedded in an alumina membrane have also been employed as electrodes for the oxygen reduction reaction, ORR, with and without the application of an external magnetic field.[13,14] In view of the

current interest in enhancing the ORR in hydrogen fuel cells without precious metals as the cathode catalyst,[15−19] our goal here is to investigate the effect of the nonuniform magnetic field produced by micrometer-scale magnetic particles. We create substrates covered with discrete ferromagnetic particles of cobalt or iron, which we use as cathodes for the ORR, and compare them with similar nonmagnetic zinc particles examining their response in the presence and in the absence of an external magnetic field.

2. EXPERIMENTAL METHODS

Polyaniline (PANI) films were grown from an aqueous solution containing 0.1 M aniline, 0.1 M H_2SO_4, on gold-coated Si/SiO$_2$ substrates with an exposed area of 1.13 cm^2. Electrochemical measurements were performed with a CHI 660 potentiostat. A three-electrode arrangement was used. Platinum mesh was used as the counter electrode, and a Ag/AgCl electrode was used as a reference. The Au/Si(100) subtrates were prepared by e-beam evaporation of 20 nm of chromium followed by 40 nm of gold using a BOC Edwards Auto 500 evaporator (base pressure: 5 × 10^{-7} mbar). Prior to each electrodeposition, the surface was cleaned with H_2O_2 + 1 M KOH, followed by electrochemical stripping in deaerated 1 M KOH solution. The electropolymerization was performed potentiodynamically at 30 mV s^{-1}, with an initial activation cycle ranging from 0 to 0.9 V vs Ag/AgCl, followed by 25 successive cycles in the potential range −0.15 to 0.55 V. The resulting film was rinsed with copious amounts of water. Metallic grains were then electrodeposited potentiostatically on the electro-synthezised PANI films, employing FeSO$_4$·7H$_2$O, CoSO$_4$·6H$_2$O, or ZnSO$_4$·H$_2$O (all reagents purchased from Sigma), in the concentration range 0.045−1 M, in either 0.1 M boric acid (BA) or 0.1 M acetic acid (AA). The pH values of each bath are indicated in the text and figure captions.

Morphology and composition were studied by scanning electron microscopy (SEM), and energy dispersive X-ray analysis (EDAX) was employed to identify the elemental content of the crystal produced. Cross section images were taken after the samples were milled in a Zeiss Auriga focused ion beam (FIB) microscope. Image analysis was carried out with Image J software package. A PANalytical X'pert Pro X-ray diffractometry (XRD) system with a Cu Kα (λ = 1514.1 pm) X-ray source and an X'celerator IP detector was used to characterize the crystal structure of the metallic grains. Magnetization measurements were carried out in a 5 T Quantum Design SQUID magnetometer at room temperature.

The oxygen reduction reaction (ORR) was characterized on several of the metallic cluster-PANI substrates. Zinc, cobalt, and iron hemispheres were deposited on the substrates to minimize morphological discrepancies. The electrodeposition of Co and Fe was carried out with the electrode in horizontal position, facing upward. For zinc, the hemispheres on the electrode were prepared with the electrode in vertical position and cycling PANI 20 times. In all cases, the deposition was carried out with *iR* compensation. Solutions of the ions with a 1 M concentration were employed. Fe, Co, and Zn were potentiostatically deposited at −1.40 V, and the corresponding accumulated charges were 0.20 C, 0.30, and 0.16 C, respectively. To increase the conductivity, 10 nm of Au was first sputtered onto the surfaces using a Balzers SCD004 sputter coater. A nafion 10 wt % aqueous solution (Sigma) was used to protect the metallic grains from electrodissolution; 0.1 mL of a 1:19 diluted Nafion solution was dispersed onto each electrode and let dry. The ORR was measured for all three cathodes in an upward-facing horizontal geometry. A 1 cm^3 Nd−Fe−B permanent magnet that produced a magnetic field of approximately 360 mT at the cathode surface was placed behind the cathode in order to generate a uniform field at the zinc hemispheres and a nonuniform stray magnetic field at the iron or cobalt hemispheres. Prior to each experiment, a 0.5 M H_2SO_4 solution was bubbled with O$_2$ for at least 20 min to produce saturation. The oxygen content is estimated to be about 1 mM.[20,21] The potential was scanned at 5 mV s^{-1}, in the potential range 0.2 to −0.2 V.

3. RESULTS AND DISCUSSION

3.1. Crystallite Growth and Characterization. Electrodeposition of iron, cobalt, and zinc was carried out on the gold-coated silicon substrates modified with a potentiodynamically grown polyaniline (PANI) film. It is well-known that PANI exists in three oxidation states known as leucoemeraldine (insulating), emeraldine (conducting), and pernigraniline (insulating).[22] The potential range at which polyaniline switches from leucoemeraldine to emeralidine is ~0.20−0.25 V vs Ag/AgCl,[22] well beyond the standard redox potential for the reduction of transition metal ions to their metallic form, which is less than −0.8 V vs Ag/AgCl. This indicates that PANI is in its insulating, leucoemeraldine state while the electrodeposition of these ions is taking place. Figure 1 shows a cyclic
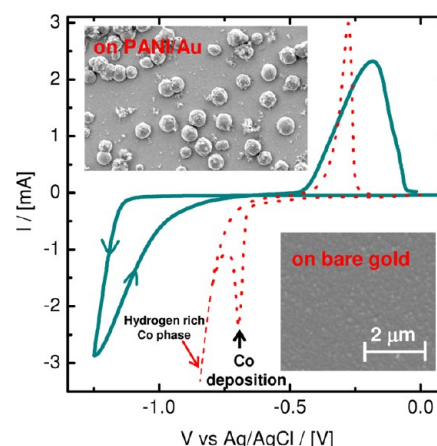

Figure 1. Cyclic voltammogram of cobalt electrodeposition onto gold (dotted line) or PANI-coated gold films (solid line): 1 M CoSO$_4$, 0.1 M H$_3$BO$_3$, pH = 4.4. Scan rate: 50 mV s^{-1}. Geometric area: 1.13 cm^2. Insets: SEM images of cobalt deposits obtained potentiostatically at −1.40 V on PANI (top left) and at −1.10 V on bare gold (bottom right). The particles at the top were obtained after passing 0.20 C.

voltammogram for the electrodeposition of cobalt on PANI/Au. During the cathodic scan, it can be seen that the reduction process starts at about −1.10 V, well below the standard value for cobalt (~−0.5 V). On the reverse scan, the current is higher, and it reaches zero near −0.70 V, giving rise to a crossover between the cathodic and anodic branches. Crossovers are a consequence of interfacial affinity between the substrate and the electrodeposits,[23,24] and in this case, it can also be understood in terms of a kinetically inhibited reaction. The current in this voltammogram is much smaller than we would normally expect for the conditions employed; the concentration of Co^{2+} in the electrolyte is 0.9 M, the scan rate is 50 mV s^{-1}, and the electrode geometrical area 1.13 cm^2. This is the case of the voltammogram shown in red. Cobalt deposition starts at −0.7 V, followed by a hydrogen rich cobalt deposit.[25] If the whole surface area were active, the current would be ~30 times larger. The insulating nature of PANI in this potential region hinders the metal deposition, thereby decreasing the current and shifting the deposition potential to a more negative value. During the reverse scan, the current is larger since cobalt is no longer being deposited on insulating PANI/Au but onto the cobalt grains already formed, which is, of course, a more favorable process. In the insets of Figure 1 are shown SEM images corresponding to the electrodeposits obtained on PANI/Au (top left) and on bare Au (bottom

right). It can be seen that discrete particles are obtained when the electrodeposition is performed on PANI/Au and a continuous film is obtained when the electrodeposition is carried out on bare gold. It appears that cobalt nucleates at pinholes within the polymer and that these nuclei grow to form larger grains. Once growth begins, the cobalt builds up preferentially on the cobalt grains rather than on the PANI film.

The concentration of the ion and the nature of the acid present in the electrolyte are key factors determining the shape of the grains obtained. Iron, cobalt, and zinc grains were all deposited from 1 M, 0.2 M and 45 mM solutions, in the presence of 0.1 M acetic acid (AA) or 0.1 M boric acid (BA). Figure 2 shows various SEM images of cobalt electrodeposits
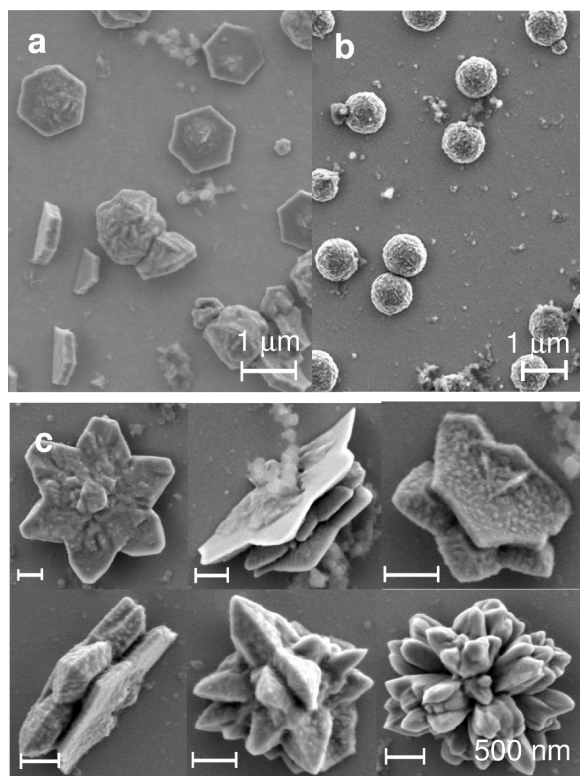
Figure 2. Effect of Co^{2+} concentration and acid on the crystal habit of cobalt grains. SEM images of cobalt particles electrodeposited from (a and b) 0.2 M $CoSO_4$ and (c) 45 mM $CoSO_4$. The solutions used in a and c also contain 0.1 M H_3BO_3, and that used in b contains 0.1 M acetic acid. pH values are (a) 4.4, (b) 3.1, and (c) 4.7. The cobalt grains were produced potentiostatically at −1.40 V. Charge deposited is 0.20 C. Scale bars in c correspond to 500 nm.

obtained with a 0.2 M (Figure 2a, b) and 45 mM (Figure 2c) Co^{2+} concentration. When the concentration of Co^{2+} is ∼0.2 M, well-formed hexagons are mainly observed with 0.1 M BA (Figure 2a), while hemispheres are obtained with 0.1 M AA (Figure 2b). This effect has also been seen in cobalt particles, where their crystal habit is determined by the presence of different surfactants, and by the concentration of the precursor.[26] Figure 3a shows XRD patterns of these Co samples. The data in red and green correspond to samples deposited in the presence of BA and AA, respectively. It can be clearly seen that the XRD patterns of these two types of samples are different. For the samples produced with BA, only three major reflexions arising from the 002, 101, and 004 planes of the hexagonal structure of cobalt are present. The ratio of the
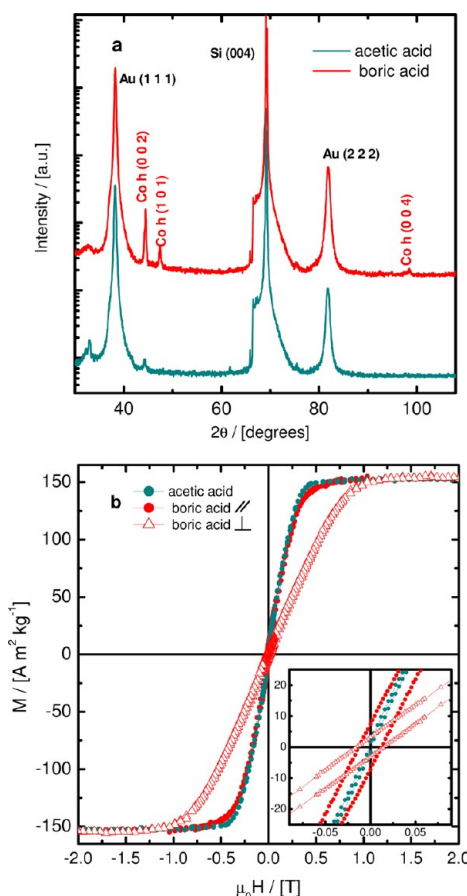
Figure 3. Effect of acetic acid on the cobalt crystal phase. (a) XRD patterns and (b) magnetization loops of cobalt grains obtained from 0.2 M $CoSO_4$ baths, with acetic acid (green) and boric acid (red). With boric acid, cobalt is mainly in its hexagonal phase, which produces different saturation when the magnetic field is applied parallel (circles) or perpendicular (triangles) to the substrate. The inset shows a magnification of the hysteresis loop near zero field.

intensities of the 002 to the 101 reflexions is 5.3:1, while for randomly oriented powders this ratio is 0.28:1. This confirms that the c-axis has a strong preferred orientation normal to the c plane of the substrate, with the growth mode occurring in the c-plane, parallel to the substrate surface. There is also a small amount of the cubic phase. The coherence length in the 002 plane calculated using Scherrer's formula is 82 ± 3 nm, which is in agreement with the observed thickness of the cobalt hexagons in the c direction, indicating that they are indeed monocrystals. The XRD pattern of samples fabricated in the presence of AA is shown by the green line in Figure 3a. There is only the one reflection located at ∼44.3 whose intensity is very low. The crystallite size calculated from this reflection is 55 ± 3 nm, much smaller than the micrometer-size particles seen by SEM. Therefore, not only has the morphology been modified but they also have a different polycrystalline structure than the monocrystalline hexagons. The hemispheres are similar to the ones produced at high concentrations of Co^{2+} in the absence of AA (compare Figure 2b, and Figure 1 inset, top), which exhibit a similar XRD pattern. The origin of the change in the crystal habit and crystallinity of cobalt when AA is present in the bath could be attributed to a change in pH and/or preferential adsorption of carboxylate groups on the different facets of the grains. In electrodeposited films, current density, pH, and

carboxylated additives influence the texture of the metals produced.[27−29] In the particular case of Co, these variables also control the relative amounts of *hcp* and *fcc* phases.[29] Given that it is well-known that these two phases are magnetically different as regards anisotropy,[29,30] magnetization loops were recorded to analyze the behavior of these samples. Figure 3b compares the room temperature magnetization curves obtained with BA or AA in the bath. The saturation magnetization (M_s) in both cases is 154 A m^2 kg^{-1}, which is close to the bulk value for Co of 160 A m^2 kg^{-1}, indicating that there can be only a few nanometers of oxide at the surface of these grains. The magnetization loops of samples produced with AA or at a high concentration of Co^{2+} do not show any hysteresis, indicating that they are magnetically isotropic (see Figure 3b, green curve). Indirect evidence that the hemispheres may be mainly *fcc* cobalt is the fact that magnetocrystalline anisotropy energy of *hcp* Co is 10 times larger than that of the *fcc* phase.[29,30] The anisotropy of the hexagonal phase arises from the preferred orientation of the magnetic moment. A typical value of coercivity for these samples is $\mu_0 H_c$ = 25 mT with a remanence ratio M_r/M_s = 5%, as shown in the inset. We have found that these two values are enhanced for samples produced at lower overpotentials. At −1.2 V, the coercivity for the sample prepared in BA is $\mu_0 H_c$ = 37 mT with a remanence ratio M_r/M_s = 16.6%, while the sample prepared in AA, has a coercivity value of 3 mT and M_r/M_s = 2.5% (see the Supporting Information). Here, μ_0 is the magnetic constant 4π 10^{-7} T m A^{-1}. The value of H_c depends critically on the crystal structure and shape of the cobalt crystallites. For *hcp* cobalt nanowires, the reported coercivity is ~20 mT,[31] while for dendritic nanoparticles the value of H_c lies in the range 15−50 mT.[32] To determine the preferred orientation of the magnetic moment in the hexagonal phase (samples like the ones shown in Figure 2a), the magnetization was measured at room temperature with the magnetic field applied in two directions, parallel and perpendicular to the substrate surface. The fact that the magnetization saturates more easily when the magnetic field is applied parallel to the substrate shows that the spins are oriented in the *c*-plane of the hexagonal crystals (parallel to the substrate),[33] despite the fact that the magnetocrystalline anisotropy of cobalt K_1 = 500 kJ m^{-3} favors the *c* axis. This indicates that shape anisotropy is the dominant contribution for the hexagons. The effective anisotropy constant, K_{eff}, can be calculated from the anisotropy field H_a deduced by extrapolating to saturation the hard axis magnetization curve, measured with the magnetic field perpendicular to the surface. The value obtained using the expression $H_a = 2K_{eff}/\mu_0 M_s$ with M_s = 1.35 MAm^{-1}, is K_{eff} = −506 kJ m^{-3} (the negative sign indicates easy-plane anisotropy). The shape anisotropy, K_{sh}, for the thin platelets with demagnetizing factor $\mathcal{N}$ is $K_{sh} = [(1 − 3\mathcal{N})/4]\mu_0 M_s^2$, so the effective anisotropy expected for the hexagonal cobalt platelets is $K_{eff} = K_{sh} + K_1$; with $\mathcal{N}$ = 0.9 K_{eff} = −1030 + 500 = −530 kJ m^{-3}.[33] This is in agreement with our measurements. The difference can be attributed to the misalignment of some of the Co platelets, which are oriented with their faces perpendicular to the surface. The in-plane and out-of-plane magnetization loops of samples produced with AA are equivalent, indicating that there is no magnetization difference given by shape anisotropy. This is in agreement with the SEM images showing hemispheres whose diameter and height are similar.

Since the pH of the baths employed to produce the particles shown in Figure 2a and b are different, (4.4 in Figure 2a and 3.1

Figure 2b), the change in texture might be caused by the adsorption of hydrogen and hydrogen evolution processes.[27−29] It could also be a consequence of adsorption of carboxylate groups of AA onto the crystal surface, since semihydrophilic molecules modify the shape of electrodeposits because they preferentially adsorb onto certain crystal facets, thereby controlling the growth rates along different crystal axes.[26,34−36] To distinguish between these two processes, a solution containing 0.1 M acetic acid-acetate buffer (pH = 4.4) was employed to prepare microparticles. Hemispherical particles are obtained in either AA or AA/acetate buffer baths, and little influence of pH is observed. The magnetization loops also show soft magnetic behavior with no coercivity. Therefore, AA present in the bath inhibits the in-plane growth of hexagons or stars, and hemispheres are produced instead (results are shown in the Supporting Information).

Decreasing the Co^{2+} concentration to about 45 mM, gives rise to interesting star-like microcrystals. Figure 2c shows a series of these unique structures, while in the Supporting Information there is an SEM overview of this type of sample. At low Co^{2+} concentrations, depletion of electroactive species at the surface of the grains leaves a zone at the edge of the crystal that is more concentrated in Co^{2+} ions, enhancing in this way the growth rate of the edges.[34,35] Furthermore, the growth tends to be fastest in the directions where the atoms are least dense-packed, which are the ⟨110⟩ directions for cobalt. Therefore, a hexagonal nucleus grows into a six-pointed star.

The effect of concentration and the acid present in the bath on iron particles is depicted in Figure 4. The images at the top correspond to deposits obtained with a 1 M FeSO$_4$ solution. Whereas in the case of cobalt, hemispheres were obtained when AA was present in the electrolyte, here the presence of AA favors the formation of well-defined submicrometer size cubes (Figure 4b) and it is with BA that hemispheres are found
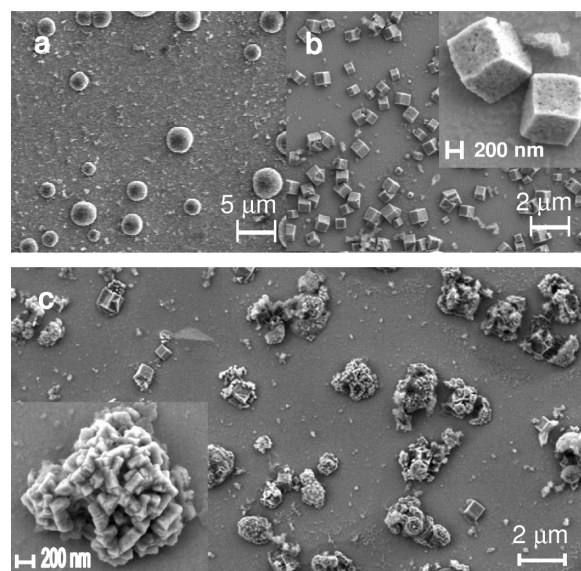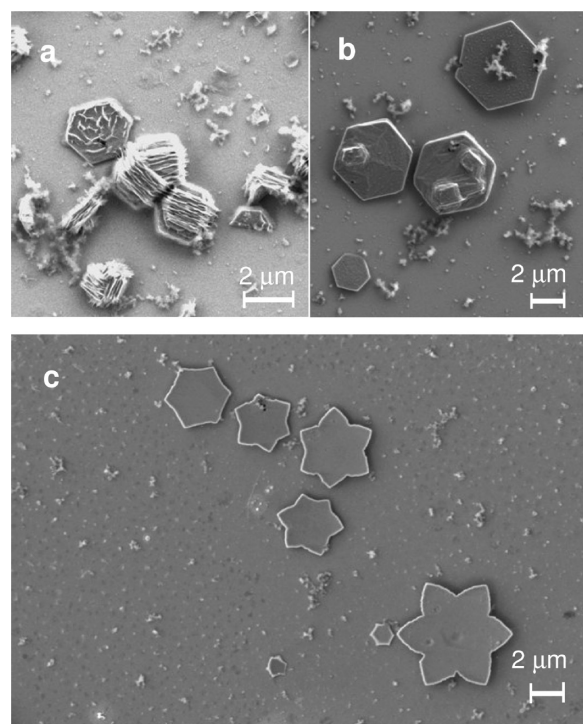

Figure 4. Effect of Fe^{2+} concentration and the acid present in the electrolyte on the crystal habit of iron grains. SEM images of iron particles electrodeposited from (a and b) 1 M FeSO$_4$ and (c) 45 mM FeSO$_4$. The solutions used in a contain 0.1 M boric acid, and those used in b and c contain 0.1 M acetic acid. pH values are (a) 3.0, (b) 2.7, and (c) 2.9. Iron crystals were produced potentiostatically at −1.60 V on PANI films. Inset in b is a high magnification image of iron cubes showing their porous structure.

instead (Figure 4a). In this case, the pH for both 1 M $FeSO_4$ solutions are alike, (2.7 for AA and 3.0 for BA) even though the acid dissociation constant of AA and BA are quite different (1.75×10^{-5} and 5.81×10^{-10}, respectively).[37] The acidity of these solutions is given by the presence of a small percent of Fe^{3+} in fresh Fe^{2+} solutions, which is much more acid than AA or BA alone, with a hydrolysis constant value of 6.45×10^{-3}.[38] Therefore, the change in the crystal habit of this crystal cannot be explained in terms of hydrogen evolution and adsorption of hydrogen, given that the proton concentration in the baths is alike. Hence, it is the specific interaction between the carboxylic group of AA and the iron surface that leads to a change in crystal habit. Magnetic measurements of substrates containing Fe particles reveal that the samples are easily oxidized by air; M_s of a freshly prepared sample is $\sim$170 A m^2 kg^{-1}, with $\mu_0 H_c = 3$ mT, compared with the bulk iron value of 220 A m^2 kg^{-1}. After a day, M_s has decayed by $\sim$40%. XRD patterns show only the reflection corresponding to the 110 plane of body-centered cubic lattice. In the case of cubes, the coherence length obtained from this reflection is 25 nm, indicating that these cubes are less ordered than the zinc and cobalt particles. For the hemispheres, the value is 18 nm. In the inset of Figure 4b, it is seen that these iron cubes are actually porous. This crystal habit was still sustained when 0.1 M Fe^{2+} solutions were employed. Lower concentrations yielded more dendritic-like structures, as shown in Figure 4c. These structures are much more open, consisting of an array of smaller cubes growing in all directions. Figures with magnetization loops and XRD diffraction patterns of iron samples can be found in the Supporting Information.

Zinc crystals were also produced by electrodeposition on the PANI-coated substrates. The effect of AA and Zn^{2+} concentration is depicted in Figure 5. The two images at the top correspond to particles obtained with a 1 M $ZnSO_4$ solution. On the left are the particles obtained with BA and on the right with AA. It can be seen that AA does not completely change the crystal habit of these particles; in both cases, the crystals are hexagons but the AA has a smoothing effect. The faces are better defined with AA, whereas in its absence the grains are quite rough and laminated. The XRD patterns of Zn-PANI films, which can be found in the Supporting Information, show four major reflexions corresponding to the 002, 101, 004, and 202 planes of the hexagonal lattice. As in the case of Co, Zn forms hexagonal crystals oriented parallel to the polymer surface, with some edge-on growth. The coherence length of the c direction, 56 $\pm$ 4 nm, is similar to the observed thickness of the zinc hexagons along the c-axis. The ratio of the intensities of the 002 to the 101 reflexions is 95, much larger than the corresponding value found for cobalt. At lower Zn^{2+} concentrations, the preferred alignment of the c-plane with the surface of PANI is sustained, although the hexagons now grow in star-like shapes, due to preferential growth of the least densely packed planes, which leads to most rapid growth in the $\langle 110 \rangle$ directions. The atomic packing is denser in the (110) plane by a factor $2/\sqrt{3}$ than the (100) plane.

The metallic crystals electrodeposited on PANI films can be removed from the substrate by wetting the surface with a few microliters of toluene and then immersing the sample in ethanol. The magnetic particles can then be collected with a magnet, as shown in Figure 7S in the Supporting Information. These cobalt particles could be employed as a catalyst in hydrogenation reactions of several organic compounds,[39−42]


Figure 5. Effect of Zn^{2+} concentration and the acid present in the electrolyte on the crystal habit of iron grains. SEM images of zinc particles electrodeposited from (a and b) 1 M $ZnSO_4$ and (c) 50 mM $ZnSO_4$. The solutions used in a contain 0.1 M boric acid, and those used in b and c contain 0.1 M acetic acid. pH values are (a) 4.5, (b) 2.8, and (c) 3.4. Zinc crystals were potentiostatically electrodeposited at −1.40 V on PANI films. The charge passed in all cases is 0.20 C.

where well-defined reactive crystalline facets are crucial in controlling catalytic properties or in magnetic bioseparation.[42−47]

As well as concentration and additives, the orientation of the electrode modifies the crystal habit of the electrodeposited particles because gravity influences the convection of electro-active species in the vicinity of the electrode surface. Although we do not discuss this topic in detail here, it is important to mention it because it will be used to produce hemispheres of Zn, which are important for the next section of our work.

3.2. Magnetic Field Effects on the Oxygen Reduction Reaction. The reduction of O_2 to H_2O is a four-electron process, although depending on the electrode material, O_2 might first be reduced to H_2O_2. This reaction is kinetically slow because it involves breaking of the double bond between the two atoms in the oxygen molecule. Chemical interactions between O_2 and some electrode materials stabilize the formation of intermediate species, thereby increasing the reaction rate and reducing the formation of H_2O_2. Besides the choice of electrode material, it may be possible to exploit magnetic fields to influence the reduction reaction.[7−13] To make a fair comparison, substrates containing similar hemispheres of Fe, Co, and Zn with a mean diameter of $\sim$2.3 μm, coated with 10 nm of gold were used to evaluate the magnetic field effect produced by the magnetic micrograins on the oxygen reduction reaction (ORR). PANI is necessary to produce these microstructured substrates. Its conductivity however, is switched off in the potential region where the metallic grains are stable (from −0.15 V vs Ag/AgCl). To enhance the conductivity, the substrate is coated with Au,
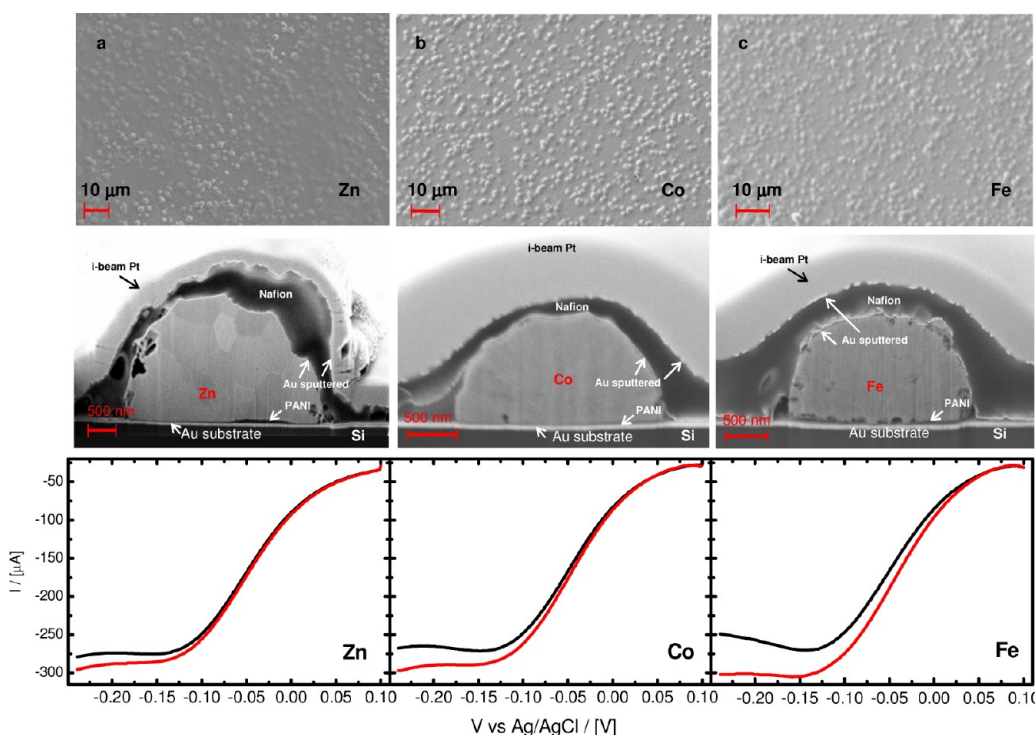
Figure 6. Morphology of substrates modified with microhemispheres and the influence of magnetic field gradients on the oxygen-reduction reaction. (a) Zn, (b) Co, and (c) Fe. The upper row shows top views of the electrodes. The middle row shows cross-sectional images of the metallic grains indicating the layered structure. The bottom row shows cathodic scans for the ORR. Red curves correspond to the voltammetric response recorded when a permanent magnet is positioned behind the silicon substrate. The thickness of the substrates is 0.7 mm. The substrates containing the metallic grains were coated with 10 nm of Au, followed by Nafion. Scan rate: 5 mV s^{-1}. Geometric area: 1.13 cm^2. O$_2$-saturated 0.5 M H$_2$SO$_4$ solution.

which is also useful because it prevents the oxidation of Fe grains on extended exposure to atmospheric oxygen. However, we found that, after Au coating, some of the surface of the transition metal grains was still exposed to the solution and needed to be protected with a Nafion layer to prevent electrodesorption. Nafion is widely employed as a cation exchange membrane and as an anion insulator, which prevents the oxidation and dissolution of metallic particles.[48] In the Supporting Information, there is a detailed presentation of cathodic scans corresponding to the ORR response on bare gold, PANI, and the effect of Nafion and gold layers, with and without the grains.

Figure 6 includes the morphological characterization of the metal particles and the cathodic scans for the ORR recorded at 5 mV s^{-1}, for the different cathodes. Each column shows the corresponding images and voltammetric scans obtained for Zn, Co and Fe. The top row shows SEM images of each electrode surface. To be able to image by SEM, another 10 nm Au layer was sputtered on top of the Nafion layer. It can be seen that, in all cases, after the Nafion coating the grains still protrude from the surface. The hemispheres range from 1.6 to 3 μm diameter, with roughly ~4.1 million particles cm^{-2} for Zn, ~3.7 million for Co, and ~3.9 million for iron. The middle row in Figure 6 shows cross-section images of the grains on each substrate, which were milled with a focused ion beam (FIB) system. The layers that can be distinguish are as follows: at the bottom the silicon substrate, then 40 nm Au that was sputtered onto Si and used as the electrode to produce PANI, then the PANI film whose thickness ranges from 10 to 80 nm across the electrode surface, then the metal grains, the thin Au layer sputtered on top of the hemispheres and the PANI, the Nafion layer with a

thickness between 200 and 500 nm, then another Au sputtered layer (added to visualize the film), and finally the i-beam deposited Pt stripe that protects the structure during milling. A hexagonal polycrystalline structure is evident for the Zn hemisphere; Co appears featureless, while the Fe hemisphere seems to have a more porous structure.

The hemispherical particles were chosen to minimize differences in morphology when evaluating the effect of an external magnetic field on the ORR. Zinc is diamagnetic but cobalt and iron are soft ferromagnetic materials. Therefore, in the absence of an external magnetic field, the remanent magnetic moment for Co or Fe particles is very small and they create little or no stray magnetic field. An external magnetic field is necessary to induce magnetization in the Co or Fe. The field is produced by a 1 cm^3 Nd−Fe−B permanent magnet positioned behind the substrate. The 360 mT stray field produced by the magnet is sufficient to induce more than half the saturation magnetization of the Fe or Co particles present on the substrate. At the bottom of Figure 6 are cathodic scans obtained with the substrates containing Zn, Co, and Fe hemispheres. The voltammetric response obtained with the three different substrates in the absence of an external magnetic field is comparable; the peak current is ~230 μA and peak potential is ~−0.15 V. This indicates that the ORR is comparable in the three cases. When the magnet is in position, an overall increase of the current is observed. This enhancement is different for each metal: 3.0 ± 0.7% increase in the current is observed with zinc, 7.8 ± 1.2% with Co, and 11.6 ± 1.8% with Fe. There is also a slight increase in the current at voltages < −0.15 V. This is likely to be the second reduction step of H$_2$O$_2$ to H$_2$O.

The increase observed with Zn can be attributed to the Lorentz force, arising from the interaction between the external magnetic field and the local current density. Although this force should be at its minimum value given that the magnetic field and the electric field are parallel to each other, the curved equipotential at the surface of the metallic grains give rise to a perpendicular component of the electric field. However, the $\sim$12% increase in current observed when iron grains are on the substrate and $\sim$8% with cobalt grains cannot be explained only by the Lorentz force, given that the morphology of these substrates is similar to that of Zn. The effect of the external field on the Fe or Co is to magnetize the metal particles and create a highly nonuniform stray field in their vicinity. Molecular O_2, with its two unpaired electrons in antibonding $\pi*$ orbitals, is a paramagnetic molecule with a spin $\Sigma = 1$, which raises the possibility that O_2 might be attracted toward the surface of the magnetic particles. Based on the Curie-law susceptibility,[33] the ratio of the magnetic stabilization energy $-^1/_2\langle m \rangle B$ to the thermal energy kT is $-^4/_3(\mu_B B/kT)^2$, which is of order 10^{-6}. Here, $\langle m \rangle$ is the thermal average of the oxygen magnetic moment in the field B, μ_B is the Bohr magneton, k is Boltzmann's constant, and T the absolute temperature. There is therefore a negligible change in the equilibrium concentration of oxygen due to the magnetic field.

Another argument can be made in terms of forces. The field gradient force $F_K = (1/2 \, \mu_0)\chi_m c \nabla B^2$ tends to drag paramagnetic species into the magnetic field, and it may become significant when the gradient of the mangetic field is very large. In this equation, χ_m is the molar susceptibility and c the concentration of paramagnetic species in the electrolyte, in mol m^{-3}. In the present case, the saturated O_2 concentration is about 1 mol m^{-3},[20,21] and the molar susceptibility for $\Sigma = 1$ and $g = 2$ is $\chi_m = 8 \, \mu_0 N_a \mu_B^2/3kT$, where N_a is the Avogadro's number. The value of χ_m at room temperature is therefore 4.2×10^{-8} m^3 mol^{-1}; hence, if ∇B^2 is $\sim 10^5$ T^2 m^{-1} for these micrometer-size particles, the field gradient force is 1.6×10^3 N m^{-3}. ∇B^2 is calculated considering that the external magnetic field is 360 mT, the magnetic polarization of Co or iron is 1.6 and 2.2 T, and the size of the particles is 2 μm. This is negligible compared to the force $F_d = RT\nabla c \sim 10^7$ N m^{-3}, driving diffusion of oxygen toward the cathode.

Nonetheless, a local magnetic field indubitably influences electrode reactions when paramagnetic species are involved. This is seen in studies of electrodeposition of 3d metals.[9−13] Recently, this was demonstrated for electrodeposition of copper, which is increased several fold by a field of about 300 mT produced by an array of small permanent magnets backing the cathode, even from very dilute, 10 mM, Cu^{2+} solutions.[11] The susceptibility of a 1 mM O_2 solution is 4/15 of that of 10 mM Cu^{2+}, so similar arguments apply. The point is that the field gradient force F_K is quite comparable to the buoyancy forces driving convection, which ultimately controls the electrode reaction in the mass-transport limited regime, via the extent of the diffusion layer.

The current density at the peak in Figure 6 is $\sim$2.4 A m^{-2}, so the diffusion layer thickness, δ, is given by the equation $j_c = nFD\nabla c$, where $n = 2$, F is Faraday's constant, $D \sim 10^{-9}$ m^2 s^{-1}, and $\nabla c = ^c/_\delta$. This gives a value of $\delta = 90$ μm, which is much greater than the interparticle separation and the overall roughness of the cathode surface. Although it does not influence diffusion, the field gradient force is able to influence convection provided there is a paramagnetic concentration gradient established in the perpendicular direction.[9−13] This is

why this force only becomes important when a concentration gradient is produced by the electrochemical reaction at the electrode surface, and it is maximum when ∇B^2 is perpendicular to the concentration gradient ∇c. The induced convection increases the flux of paramagnetic species toward the surface of the grains, and the current is enhanced as a result. Tschulik et al. show plots of numerical simulations of this type of flow during electrodeposition of copper where the influence of a high magnetic field gradient on the flow velocity of paramagnetic species is demonstrated.[13]

A practical application of this magnetically induced convection can be envisaged if nanosize magnetic catalysts such as some perovskites[17,49] or Fe$_3$O$_4$ are employed as electrode components with high active surface area in hydrogen fuel cells, which could see a 2-fold enhancement of the current if most of the electrode surface is covered with these particles.

4. CONCLUSIONS

Metallic crystals of iron, cobalt, and zinc can be produced by electrodeposition on PANI films. Iron grows as submicrometer cubes, which are ferromagnetic but easily oxidized. The crystal structure and shape of the cobalt grains depends on the concentration of Co^{2+} in solution and the presence of acetic acid in the electrolytic bath. Cobalt hexagons, with a high surface area of 001 facets and in-plane magnetization are produced from 0.2 M Co^{2+} solutions, with BA. When AA is present in the electrolyte, polycrystalline hemispherical particles are obtained instead of hexagons. All iron deposits have a body-centered cubic crystal structure, exhibiting a cubic shape in the presence of AA and hemispheres in the presence of BA. The ferromagnetic Fe or Co particles can be removed from the substrate and could be employed for general catalytic purposes[39−42] or in magnetic bioseparation.[43−47]

Zinc hexagons can be produced by electrodeposition onto PANI films, and the presence of AA suppresses the growth in the c direction. The hexagonal crystals grow in the c-plane, parallel to the substrate, with a growth rate up to 100 times greater than along the c axis. Low concentrations of the active ion give rise to star-shaped particles with dendritic-like growth, which tends to maximize the edge legth.

Microstructured substrates of all three metals were employed to quantify the enhancement of the current for the oxygen reduction reaction. The arrays of micrometer-size ferromagnetic particles are useful to test the effect of nonuniform magnetic fields acting at the surface of electrode materials. It was found that the current can be increased by 8 to 12% when the microparticles are magnetized with a small permanent magnet. This enhancement is due to the nonuniform magnetic stray field, which drives convection within the diffusion layer, when the field gradient at the surface of the magnetic grains and the concentration gradient of paramagnetic O_2 are perpendicular. This is an important result because it suggests that the performance of the cathode in hydrogen fuel cells could be improved with the addition of small permanent magnets and the use of nanosized ferromagnetic catalysts given that the kinetics of the ORR is only affected by the nature of the electrode material. We are currently investigating the enhancement of ORR in ferromagnetic nanocomposites where the effect may be larger since the magnetic enhancement is related to the magnetic field gradient, which at the nanometer scale can exceed 10^7 T^2 m^{-1}.

■ ASSOCIATED CONTENT

○S Supporting Information

Magnetization loops of iron cubes, XRD patterns of iron and zinc, and cathodic scans for the ORR measure on different substrates. This material is free of charge via the Internet at http://pubs.acs.org.

■ AUTHOR INFORMATION

Corresponding Author

*E-mail: aranzazl@tcd.ie.

Notes

The authors declare no competing financial interest.

■ ACKNOWLEDGMENTS

■ REFERENCES

(1) Ting, Y. P.; Neoh, K. G.; Kang, E. T.; Tan, K. L. *J. Chem. Technol. Biotechnol.* **1994**, *59*, 31−6.

(2) Wang, H.-L.; Li, W.; Jia, Q. X.; Akhadov, E. *Chem. Mater.* **2007**, *19*, 520−525.

(3) Xu, P.; Akhadov, E.; Wang, L.; Wang, H.-W. *Chem.Comm.* **2011**, *47*, 10764−10766.

(4) Tsakova, V. *J. Solid State Electrochem.* **2008**, *12*, 1421−1434.

(5) Andreoli, E.; Rooney, D. A.; Redington, W.; Gunning, R.; Breslin, C. B. *J. Phys. Chem. C* **2011**, *115*, 8725−8734.

(6) Tarver, J.; Loo, Y.-L. *Chem. Mater.* **2011**, *23*, 4402−4409.

(7) O'Brien, R. N.; Santhanam, K. S. V. *J. Appl. Electrochem.* **1997**, *27*, 573−578.

(8) Pullins, M. D.; Grant, K. M.; White, H.; S. *J. Phys. Chem. B* **2001**, *105*, 8989−8994.

(9) Mutschke, G.; Tschulik, K.; Weier, T.; Uhlemann, M.; Bund, A.; Fröhlich, J. *Electrochim. Acta* **2010**, *55*, 9060−9066.

(10) Dunne, P.; Mazza, L.; Coey, J. M. D. *Phys. Rev. Lett.* **2011**, *107*, 0245101.

(11) Dunne, P.; Coey, J. M. D. *Phys. Rev. B* **2012**, *85*, 224411.

(12) Tschulik, K.; Koza, J. A.; Uhlemann, M.; Gebert, A.; Schultz, L. *Electrochem. Commun.* **2009**, *11*, 2241−2244.

(13) Tschulik, K.; Cierpka, C.; Gebert, A.; Schultz, L.; Kahler, C. J.; Uhlemann, M. *Anal. Chem.* **2011**, *83*, 3275−3281.

(14) Chaure, N. B.; Rhen, F. M. F.; Hilton, J.; Coey, J. M. D. *Electrochem. Commun.* **2007**, *9*, 155−158.

(15) Wu, G.; More, K. L.; Johnston, C. M.; Zelenay, P. *Science* **2011**, *332*, 443−447.

(16) Liang, Y.; Li, Y.; Wang, H.; Zhou, J.; Wang, J.; Regier, T.; Dai, H. *Nat. Mater.* **2011**, *10*, 780−786.

(17) Suntivich, J.; Gasteiger, H. A.; Yabuuchi, N.; Nakanishi, H.; Goodenough, J. B.; Shao-Horn, Y. *Nat. Chem.* **2011**, *3*, 546−550.

(18) Cheng, F.; Shen, J.; Peng, B.; Pan, Y.; Tao, Z.; Chen, J. *Nat. Chem.* **2011**, *3*, 79−84.

(19) Zhou, W.; Ge, L.; Chen, Z.-G.; Liang, F.; Xu, H.-Y.; Motuzas, J.; Julbe, A.; Zhu, Z. *Chem. Mater.* **2011**, *23*, 4193−4198.

(20) Parthasarathy, A.; Srinivasan, S.; Appleby, A. J.; Martin, C. R. *J. Electrochem. Soc.* **1992**, *139*, 2530−2537.

(21) Gochi-Ponce, Y.; Alonso-Nunez, G.; Alonso-Vante, N. *Electrochem. Commun.* **2006**, *8*, 1487−1491.

(22) Li, C.; Bai, H.; Shi, G. *Chem. Soc. Rev.* **2009**, *38*, 2397−2409.

(23) Mirkin, M. V.; Nilov, A. P. *J. Electroanal. Chem.* **1990**, *283*, 35−51.

(24) Khelladi, M. R.; Mentar, L.; Azizi, A.; Sahari, A.; Kahoul, A. *Mater. Chem. Phys.* **2009**, *115*, 385−390.

(25) Gabe, D. R. *J. Appl. Electrochem.* **1997**, *27*, 908−915.

(26) Zhao, L. J.; Duan, L. F.; Wang, Y. Q.; Jiang, Q. *J. Phys. Chem. C.* **2010**, *114*, 10691−10696.

(27) Li, D. Y.; Szpunar, J. A. *Electrochim. Acta* **1997**, *42*, 47−60.

(28) Li, D. Y.; Szpunar, J. A. *J. Mater. Sci.* **1997**, *32*, 5513−5524.

(29) Gomez, E.; Valles, E. *J. Appl. Electrochem.* **2002**, *32*, 693−700.

(30) Weller, D.; Harp, G. R.; Farrow, R. F. C.; Cebollada, A.; Sticht, J. *Phys. Rev. Lett.* **1994**, *72*, 2097−2100.

(31) Cao, H. Q.; Xu, Z.; Sang, H.; Sheng, D.; Tie, C. Y. *Adv. Mater.* **2001**, *13*, 121−123.

(32) Zhu, Y.; Zheng, H.; Yang, Q.; Pan, A.; Yang, Z.; Qian, Y. *J. Cryst. Growth* **2004**, *260*, 427−434.

(33) Coey, J. M. D. *Magnetism and Magnetic Materials*; University Press: Cambridge, 2010.

(34) Daltin, A.-L.; Chopart, J.-P. *Cryst. Grow. Des.* **2010**, *10*, 2267−2271.

(35) Daltin, A.-L.; Addad, A.; Baudart, P.; Chopart, J. −P. *Cryst. Eng. Comm.* **2011**, *13*, 3373−3377.

(36) Wei, G.; Ge, H.; Huang, L.; Wu, Q.; Wang, X.; Huang, L. *Appl. Surf. Sci.* **2008**, *254*, 3425−3430.

(37) Kotrly, S.; Sucha, L. *Handbook of Chemical Equilibria in Analytical Chemistry*; John Wiley & Sons: New York, 1985.

(38) Cornell, R. M. Schwertmann, U. *The Iron Oxides: Structure, Properties, Reactions, Occurrences, and Uses*; Wiley-VCH: Weinheim, 2003.

(39) Herranz, T.; Deng, X.; Cabot, A.; Guo, J.; Salmeron, M. *J. Phys. Chem. B* **2009**, *113*, 10721−10727.

(40) Xu, R.; Xie, T.; Zhao, Y.; Li, Y. *Nanotechnology* **2007**, *18*, 055602.

(41) Chojecki, A.; Jobic, H.; Jentys, A.; Muller, T. E.; Lercher, J. A. *Catal. Lett.* **2004**, *97*, 155−162.

(42) Liu, Q.; Guo, X.; Chen, J.; Li, J.; Song, W.; Shen, W. *Nanotechnology* **2008**, *19*, 365608.

(43) Prina-Mello, A.; Diao, Z.; Coey, J. M. D. *J. Nanobiotech.* **2006**, *4*, 9.

(44) Grass, R. N.; Athanassiou, E. K.; Stark, W. J. *Angew. Chem., Int. Ed.* **2007**, *46*, 4909−4912.

(45) Gao, N.; Wang, H.; Yang, E.-H. *Nanotechnology* **2010**, *21*, 105107.

(46) Byrne, F.; Prina-Mello, A.; Whelan, A.; Mohamed, B. M.; Davies, A.; Gun'ko, Y. K.; Coey, J. M. D.; Volkov, Y. *J. Magn. Magn. Mater.* **2009**, *321*, 1341−1345.

(47) Prina-Mello, A.; Whelan, A. M.; Atzberger, A.; McCarthy, J. E.; Byrne, F.; Davies, G.-L.; Coey, J. M. D.; Gun'Ko, Y. K. *Small* **2010**, *6*, 247−255.

(48) Tan, S.; Belanger, D. *J. Phys. Chem. B* **2005**, *109*, 23480−23490.

(49) Miyazaki, K; Kawakita, K.; Abe, T.; Fukutsuka, T.; Kojima, K.; Ogumi, Z. *J. Mater. Chem.* **2011**, *21*, 1913−1917.